Quantification of Optimal Target Reliability for Seismic Design: Methodology and Application to Midrise Steel Buildings (Supplementary Document)

Kasra Habibi

M.Sc. Graduate, Center for Infrastructure Sustainability and Resilience Research, Dept. of Civil Engineering, Sharif University of Technology, Tehran, Iran

S. Saeid Hosseini Varzandeh

Ph.D. Candidate, Center for Infrastructure Sustainability and Resilience Research, Dept. of Civil Engineering, Sharif University of Technology, Tehran, Iran

Mojtaba Mahsuli

Associate Professor, Center for Infrastructure Sustainability and Resilience Research, Dept. of Civil Engineering, Sharif University of Technology, Tehran, Iran; Corresponding Author: mahsuli@sharif.edu, Phone: +98 (21) 6616-4217, Fax: +98 (21) 6601-4828

Nonlinear Model Validation

The nonlinear model discussed in Section 3.1 is rigorously validated in this section of the supplementary document. For this purpose, two structures are analyzed using the model developed herein. These structures have previously been subjected to large-scale shake table and quasi-static cyclic tests up to collapse (Karamanci 2013; Lignos et al. 2013; Karamanci and Lignos 2014). The experimental and analytical results of the latter studies are employed to validate the modeling of structural elements in this paper. Here, the same analyses are conducted on the analytical models of these structures developed in the present paper, and the results, which are labeled as "Validation model" hereafter, are compared to those of the original studies.

Fig. S1 shows this validation for the moment resisting frames (MRF). For this purpose, the four-story steel special moment frame building shown in Fig. S1(a) is modeled and analyzed. This building was tested by Lignos et al. (2013) under the Takatori ground motion recorded during the 1995 Kobe earthquake. Fig. S1(b) depicts the hysteresis loops of the structure in this analysis. In this figure, V_{base} represents the base shear of the building, and W represents its effective seismic weight. In addition, the result obtained from the shake table test is labeled as "Experimental Data," and the results of two analytical models are depicted as well: one that accounts for deterioration of the structural components and one that disregards it. As observed, the model developed in the present paper captures the deterioration of the structural members and accurately predicts the collapse, which occurs due to the buckling of the first story columns.

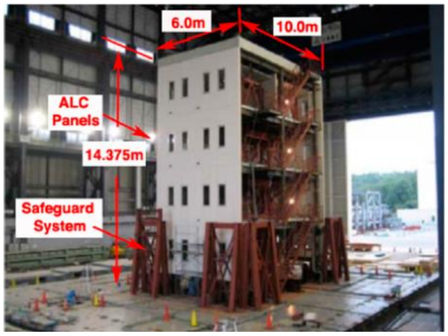

(a)

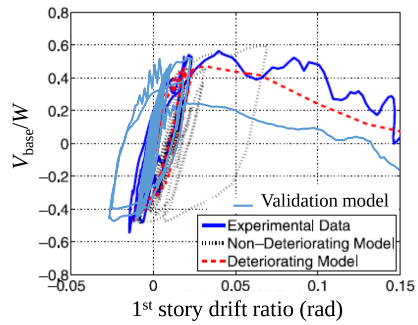

(b)

Fig. S1 Validation of the nonlinear model for MRFs: (a) the structure and (b) the hysteresis loops (Lignos et al. 2013)

Fig. S2 shows the validation for the concentrically braced frames (CBF). To this end, the two-story one-bay frame shown in Fig. S2(a) is modeled and analyzed. This frame was tested in Uriz and Mahin (2008) under a quasi-static cyclic loading protocol up to collapse. The hysteresis loops of the frame under such analysis is depicted in Fig. S2(b), in which the results of the test and an analytical model developed by Karamanci (2013) are labeled as “Experiment” and “Simulation,” respectively. Each point marked by a letter in this figure represents the initiation of a behavioral phase. Points A and B represent the time when the buckling of the first story braces occurred. Subsequently, points C and D respectively are associated with the initial and complete fracture of these braces under tension, and points E and F are those under compression. Beyond these points, the lateral resistance of the frame decreased significantly, and the remaining resistance was due to the frame action associated with the steel columns and the gusset plate beam-to-column connections. Finally, at points G and H, tearing of the first story column flanges triggered the collapse (Karamanci 2013). As observed, the model developed in the present paper is able to capture all of the behavioral phases and predicts the collapse of the frame accurately through the first story mechanism.

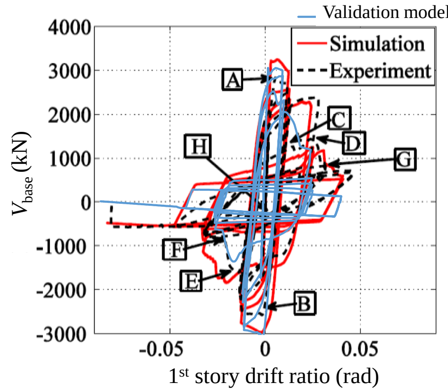

(a) (b)

Fig. S2 Validation of the nonlinear model for CBFs: (a) the structure (Uriz and Mahin 2008) and (b) the hysteresis loops (Karamanci 2013)

Supplementary Tables and Figures

This section presents the supplementary tables and figures that are referenced throughout the paper.

Table S1 Definition of the variables in the nonlinear model

Symbol	Description
E	Elastic modulus (Young's modulus) of the steel material
G	Shear modulus of the steel material
A_w	Web area of the wide-flange cross section as defined in AISC 360-10 (2010)
F_{ye}	Expected yield stress of the steel material
Z	Plastic modulus of section
L_n	Net length of the element
n	Ratio of the elastic stiffness of the rotational springs to the stiffness of the elastic element as defined in Ibarra and Krawinkler (2005)
I	Moment of inertia
I_e	Effective moment of inertia defined as $\frac{n+1}{n} \cdot I$ according to Zareian and Krawinkler (2009)
K_e	Elastic stiffness as shown in Fig. S3
M_y	Effective yield strength as shown in Fig. S3
M_p	Plastic strength which is equal to Z times F_{ye}
M_c	Capping strength as shown in Fig. S3
M_r	Residual strength as shown in Fig. S3
κ	Ratio of the residual strength to the effective yield strength as shown in Fig. S3
θ_y	Yield rotation as shown in Fig. S3
θ_p	Pre-capping plastic rotation as shown in Fig. S3
θ_{pc}	Post-capping plastic deformation capacity as shown in Fig. S3
θ_r	Residual deformation as shown in Fig. S3
θ_u	Ultimate rotation as shown in Fig. S3
Λ_s	Basic strength deterioration parameter of the modified Ibarra-Medina-Krawinkler (IMK) model (Ibarra et al. 2005)
Λ_c	Post-capping strength deterioration parameter of the modified IMK model
Λ_k	Unloading stiffness deterioration parameter of the modified IMK model
Λ_A	Reloading stiffness deterioration parameter of the modified IMK model
F_p	Ratio of the force at which reloading begins to the force corresponding to the maximum historic deformation demand according to the modified IMK model with pinched hysteretic response (Lignos and Krawinkler 2013) per Fig. S3(b)
a_h	Ratio of the reloading stiffness of the beam-to-column connection according to the modified IMK model with pinched hysteretic response per Fig. S3(b)
L_H	Effective length of braces as shown in Fig. S4(a)
N_s	Number of segments along the effective length of the brace component according to Fig. S4(a)
N_{IP}	Number of integration points of the brace component
$N_{f,w}$	Number of fibers along the width of the brace component according to Fig. S4(a)
$N_{f,t}$	Number of fibers through the thickness of the brace component according to Fig. S4(a)
ε_0	Strain amplitude at which one complete cycle of an undamaged material will cause fracture according to Fig. S4(b) and as defined in Manson (1965)
m_b	Sensitivity parameter of the total strain amplitude of the brace material to the number of cycles to fracture as defined in Manson (1965)
b_b	Strain-hardening ratio for braces with the Steel02 material (Filippou et al. 1983) according to Fig. S5
b_g	Strain-hardening ratio for gusset plates with the Steel02 material according to Fig. S5
R_0	A parameter related to the transition from the elastic to the plastic branch of the Steel02 material according to Fig. S5
cR_1	A parameter related to the transition from the elastic to the plastic branch of the Steel02 material according to Fig. S5
cR_2	A parameter related to the transition from the elastic to the plastic branch of the Steel02 material according to Fig. S5
a_2	Hardening parameter of the Steel02 material according to Fig. S5
a_1	Hardening parameter to increase the compression yield envelope of the Steel02 material after $a_2 \cdot \frac{F_{ye}}{E}$ according to Fig. S5
a_4	Hardening parameter of the Steel02 material according to Fig. S5
a_3	Hardening parameter to increase the tension yield envelope of the Steel02 material after $a_4 \cdot \frac{F_{ye}}{E}$ according to Fig. S5
L_{ave}	The average of lengths L_1, L_2, and L_3 as shown in Fig. S6
W_w	Whitmore width as defined in Hsiao et al. (2012) and shown in Fig. S6
t_g	Gusset plate thickness
L_g	Gusset plate length as shown in Fig. S6
H_g	Gusset plate height as shown in Fig. S6
γ_y	Yield shear strain as shown in Fig. S7
γ_{pz}	Shear deformation capacity of the panel zone as shown in Fig. S7
V_y	Panel zone yield strength as shown in Fig. S7
V_{pz}	Total panel zone shear strength as shown in Fig. S7
$V_{cf,y}$	Yield shear strength of the column flange as shown in Fig. S7
V_{cf}	Panel zone shear strength due to two column flanges as shown in Fig. S7
K_{cf}	Elastic stiffness of one column flange as shown in Fig. S7
$V_{cw,y}$	Yield shear strength of the column web as shown in Fig. S7
V_{cw}	Panel zone shear strength due to column web as shown in Fig. S7
K_{cw}	Shear stiffness of the column web as shown in Fig. S7
d_c	Column depth
t_{cw}	Column web thickness

Table S2 Parameters of the backbone curve for wide-flange beams of moment frames

Parameter	Value
n	10 (Ibarra and Krawinkler 2005)
K_e	$n \cdot \frac{6 \cdot E \cdot I_e}{L_n}$ (Zareian and Krawinkler 2009) further adjusted to account for the composite action of the concrete slab and the steel beam using the equivalent section method (Lignos et al. 2013)
M_y/M_p	1.17 (Lignos and Krawinkler 2011)
M_y	$\frac{M_y}{M_p} \cdot Z \cdot F_{ye}$ further adjusted to account for the composite action of the concrete slab and the steel beam as proposed by AISC 360-10 (2010)
M_c/M_y	1.11 (Lignos and Krawinkler 2011) further increased by a factor of 1.3 to account for the composite action of the concrete slab and the steel beam as proposed by NIST (2017)
M_r/M_y	0.4 (Lignos and Krawinkler 2011)
θ_p	A function of the local slenderness ratio of the beam web and the beam flange, the beam length, depth, and yield stress according to Lignos and Krawinkler (2011) further increased by a factor of 1.8 to account for the composite action of the concrete slab and the steel beam as proposed by NIST (2017)
θ_{pc}	A function of the local slenderness ratio of the beam web and the beam flange, the beam depth and yield stress according to Lignos and Krawinkler (2011) further increased by a factor of 1.35 to account for the composite action of the concrete slab and the steel beam as proposed by NIST (2017)
θ_u	0.18 (Lignos and Krawinkler 2011)
Λ_s	A function of the local slenderness ratio of the beam web and the beam flange and the beam yield stress per Lignos and Krawinkler (2011)
Λ_c	Equal to Λ_s (Lignos and Krawinkler 2011)
Λ_k	Equal to Λ_s (Lignos and Krawinkler 2011)
Λ_A	Equal to Λ_s (Lignos and Krawinkler 2011)

Table S3 Parameters of the backbone curve for wide-flange beams of braced frames

Parameter	Value
n	2.62 (Stoakes and Fahnestock 2011)
K_e	$n \cdot \frac{6 \cdot E \cdot I_e}{L_n}$ (Zareian and Krawinkler 2009) further adjusted to account for the composite action of the concrete slab and the steel beam using the equivalent section method (Lignos et al. 2013)
M_y/M_p	0.64 (Stoakes and Fahnestock 2011)
M_y	$\frac{M_y}{M_p} \cdot Z \cdot F_{ye}$ further adjusted to account for the composite action of the concrete slab and the steel beam as proposed by AISC 360-10 (2010)
M_c/M_y	1.3 (Stoakes and Fahnestock 2011) further increased by a factor of 1.3 to account for the composite action of the concrete slab and the steel beam as proposed by NIST (2017)
M_r/M_y	0 (Karamanci and Lignos 2014)
θ_p	0.055 (Karamanci and Lignos 2014) further increased by a factor of 1.8 to account for the composite action of the concrete slab and the steel beam as proposed by NIST (2017)
θ_{pc}	0.18 (Karamanci and Lignos 2014) further increased by a factor of 1.35 to account for the composite action of the concrete slab and the steel beam as proposed by NIST (2017)
θ_u	$\theta_y + \theta_p + \theta_{pc}$ (Karamanci and Lignos 2014)
Λ_s	0.9 (Karamanci and Lignos 2014)
Λ_c	Equal to Λ_s (Karamanci and Lignos 2014)
Λ_k	Equal to Λ_s (Karamanci and Lignos 2014)
Λ_A	Equal to Λ_s (Karamanci and Lignos 2014)
F_p	0.75 (Karamanci and Lignos 2014)
a_h	0.75 (Karamanci and Lignos 2014)

Table S4 Parameters of the backbone curve for wide-flange columns

Parameter	Value
n	10 (Ibarra and Krawinkler 2005)
K_e	$n \cdot \frac{6 \cdot E \cdot I_e}{L_n} \cdot \frac{\frac{G \cdot A_w}{E \cdot I_e}}{\frac{G \cdot A_w}{E \cdot I_e} + \frac{12}{L_n^2}}$ (Zareian and Krawinkler 2009; Lignos et al. 2019)
M_y/M_p	1.15 according to Lignos et al. (2019)
M_y	$\frac{M_y}{M_p} \cdot Z \cdot F_{ye}$ further adjusted to account for the bending moment-axial load interaction as proposed by AISC 360-10 (2010) and Lignos et al. (2019)
M_c/M_y	A function of the local slenderness ratio of the column web, the ratio of the laterally unbraced length of the column to its radius of gyration about the weak axis, and the ratio of its gravity-induced compressive axial load to the yield force per Lignos et al. (2019)
M_r/M_y	A function of the ratio of the gravity-induced compressive axial load to the yield force of columns per Lignos et al. (2019)
θ_p	A function of the local slenderness ratio of the column web, the ratio of the laterally unbraced length of the column to its radius of gyration about the weak axis, and the ratio of its gravity-induced compressive axial load to the yield force per Lignos et al. (2019)
θ_{pc}	A function of the local slenderness ratio of the column web, the ratio of its laterally unbraced length to its radius of gyration about the weak axis, and the ratio of its gravity-induced compressive axial load to the yield force per Lignos et al. (2019)
θ_u	0.15 (Lignos et al. 2019)
Λ_s	A function of the local slenderness ratio of the column web, the ratio of the laterally unbraced length of the column to its radius of gyration about the weak axis, and the ratio of its gravity-induced compressive axial load to the yield force per Lignos et al. (2019)
Λ_c	Equal to 90% of Λ_s according to Lignos et al. (2019)
Λ_k	Equal to 90% of Λ_s according to Lignos et al. (2019)
Λ_A	Equal to Λ_s according to Lignos et al. (2019)

Table S5 Parameters of the backbone curve for HSS columns

Parameter	Value
n	10 (Ibarra and Krawinkler 2005)
K_e	$n \cdot \frac{6 \cdot E \cdot I_e}{L_n} \cdot \frac{\frac{G \cdot A_w}{E \cdot I_e}}{\frac{G \cdot A_w}{E \cdot I_e} + \frac{12}{L_n^2}}$ (Zareian and Krawinkler 2009; Lignos et al. 2019)
M_y/M_p	1.15 according to Lignos et al. (2019)
M_y	$\frac{M_y}{M_p} \cdot Z \cdot F_{ye}$ further adjusted to account for the bending moment-axial load interaction as proposed by AISC 360-10 (2010) and Lignos et al. (2019)
M_c/M_y	A function of the column depth to web thickness ratio, its yield strain, and the ratio of its gravity-induced compressive axial load to the yield force according to NIST (2017)
M_r/M_y	A function of the ratio of the gravity-induced compressive axial load to the yield force of columns according to NIST (2017)
θ_p	A function of the depth to web thickness ratio of the column, its yield strain, and the ratio of its gravity-induced compressive axial load to the yield force according to NIST (2017)
θ_{pc}	A function of the depth to web thickness ratio of the column, its yield strain, and the ratio of its gravity-induced compressive axial load to the yield force according to NIST (2017)
θ_u	0.15 (NIST 2017; Lignos et al. 2019)
Λ_s	A function of the depth to web thickness ratio of the column, its yield stress, and the ratio of its ultimate compressive axial load to the yield force according to Lignos and Krawinkler (2010)
Λ_c	Equal to Λ_s (Lignos and Krawinkler 2010)
Λ_k	Equal to Λ_s (Lignos and Krawinkler 2010)
Λ_A	Equal to Λ_s (Lignos and Krawinkler 2010)

Table S6 Model parameters for braces, gusset plates, and panel zones

Parameter	Value
ε_0	A function of the global and the local slenderness ratio of the brace cross section and its yield strain according to Karamanci and Lignos (2014)
m_b	-0.300 (Karamanci and Lignos 2014)
N_s	8 (Karamanci and Lignos 2014)
N_{IP}	5 (Karamanci and Lignos 2014)
$N_{f,w}$	10 (Karamanci and Lignos 2014)
$N_{f,t}$	4 (Karamanci and Lignos 2014)
b_b	0.001 (Karamanci and Lignos 2014)
b_g	0.01 (Hsiao et al. 2012)
R_0	22.0 (Karamanci and Lignos 2014)
cR_1	0.925 (Karamanci and Lignos 2014)
cR_2	0.250 (Karamanci and Lignos 2014)
a_1	0.03 (Karamanci and Lignos 2014)
a_2	1.000 (Karamanci and Lignos 2014)
a_3	0.020 (Karamanci and Lignos 2014)
a_4	1.000 (Karamanci and Lignos 2014)
γ_{pz}	A function of the yield strain of the steel material and the ratio of the depth of the beam to the flange thickness of the column further adjusted to account for the column axial load effect on reducing the capacity of the panel zone according to Kim et al. (2015)

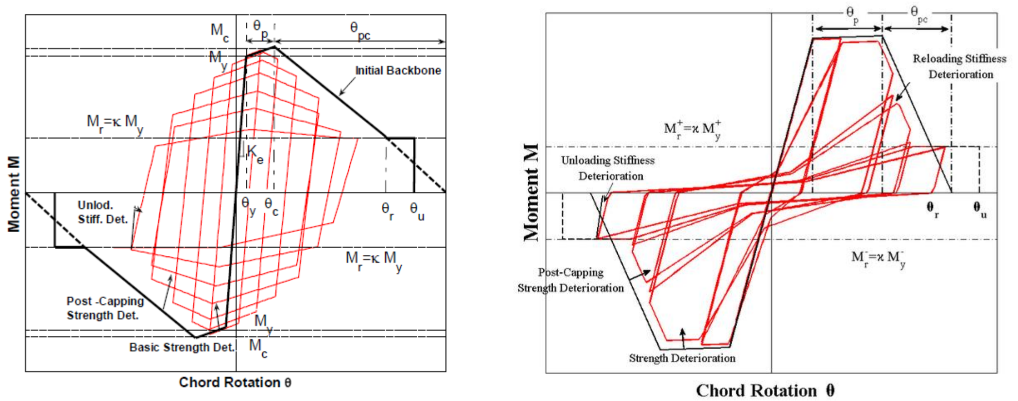

(a) (b)

Fig. S3 Modified IMK model with: (a) bilinear (Lignos and Krawinkler 2011) and (b) pinched (Lignos and Krawinkler 2013) hysteretic response

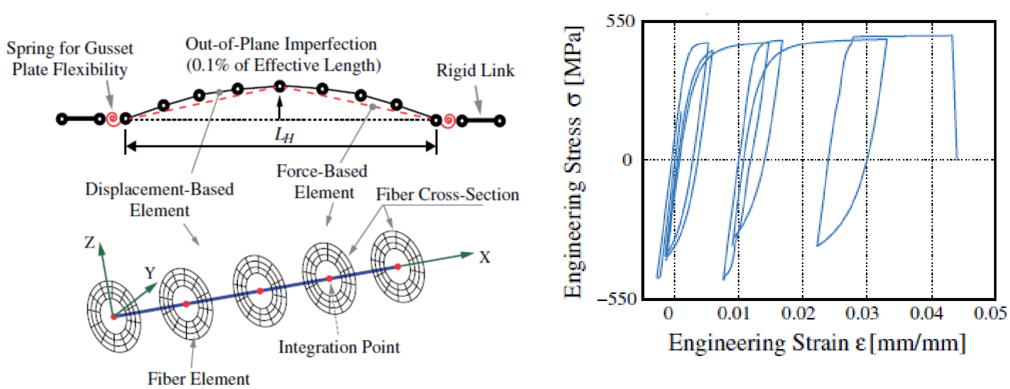

(a) (b)

Fig. S4 Steel brace model: (a) geometry and (b) stress-strain diagram (Karamanci and Lignos 2014)

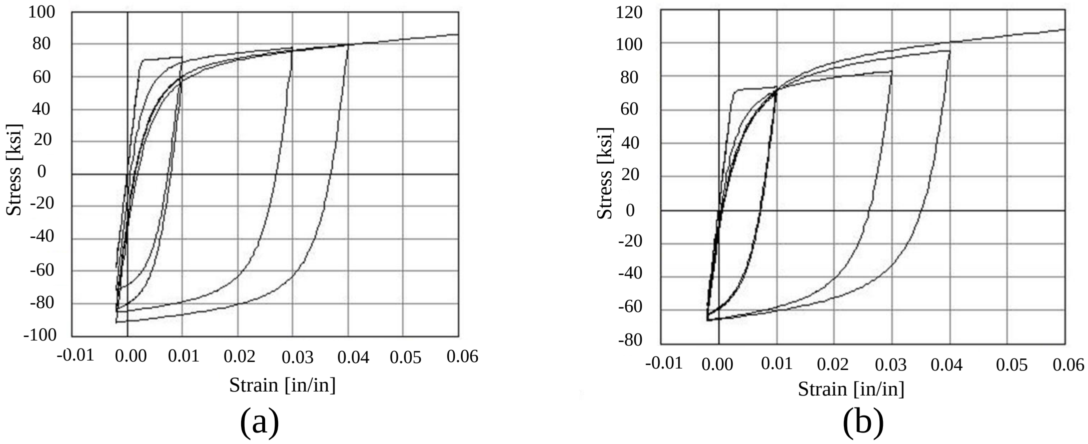

Fig. S5 The hysteretic behavior of Steel02 material with isotropic hardening (a) in compression and (b) in tension (Filippou et al. 1983) used to model steel braces and gusset plates behavior

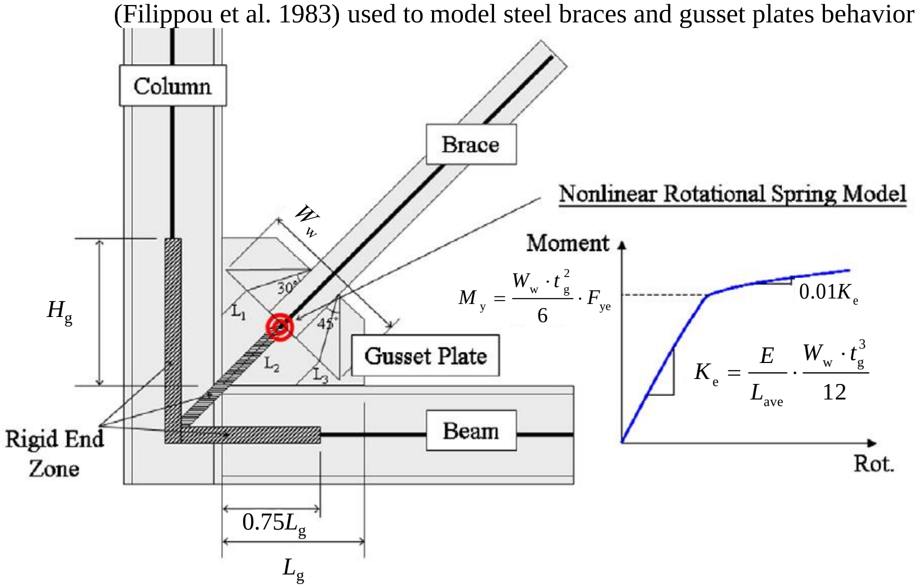

Fig. S6 Gusset plate model (Hsiao et al. 2012)

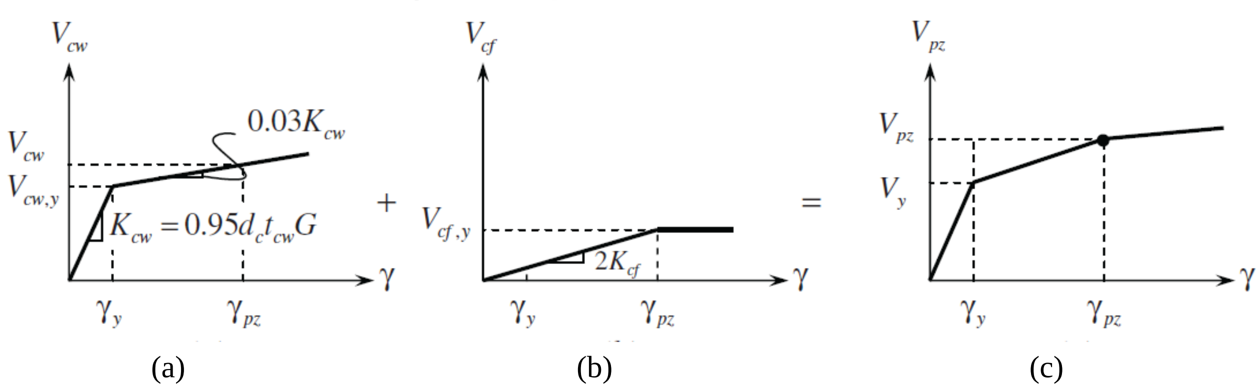

Fig. S7 Superposition of (a) column web behavior and (b) column flange behavior, which results in (c) panel zone behavior (Kim et al. 2015)

Table S7 Definition of the seismic source parameters

Symbol	Description
$\lambda_{o,i}$	Source *i* annual occurrence rate
a_i	Intercept parameter as defined in Gutenberg and Richter (1944) for source *i*
$b_i^{'}$	Distribution parameter for the magnitude model of source *i* as defined in Gutenberg and Richter (1944)
$d_{\text{centroid},i}$	Source *i* rupture plane centroid depth
$M_i^{\min}$	Source *i* minimum magnitude taken as 4.5 and 5.5 (M_w) for area and line sources, respectively per Mahsuli et al. (2019) and Rahimi and Mahsuli (2019)
$M_i^{\max}$	Source *i* maximum magnitude
$d_{\text{lower},i}$	Source *i* lower seismogenic depth
$d_{\text{upper},i}$	Source *i* upper seismogenic depth

Table S8 Area source parameters (Askari and Mahsuli 2020)

Source number *i* per Fig. 5	a_i	b_i'	$d_{\text{centroid},i}$ (km)	$M_i^{\max}$ (M_w)	$\lambda_{o,i}$
1	4	1	13.2	7.6	0.31625
2	3	0.75	13.2	7.6	0.42173
3	3.35	0.85	13.2	7.7	0.33499
4	3.5	1	13.2	7.6	0.10001
5	3	0.8	13.2	7	0.25121
6	4	1	13.2	7	0.31625
7	4	1	13.2	7.6	0.31625
8	3.9	1	13.2	7.6	0.25121
9	3	0.75	10	7.6	0.42173
10	3.35	0.85	13.2	7.6	0.33499
11	3.35	0.85	5	7.6	0.33499
12	4	1	13.2	7.6	0.31625
13	4	1	10	7.6	0.31625
14	4.5358	1.0576	10	7.4	0.5979
15	3.5	0.86	13.2	7.6	0.42661
16	3.35	0.85	13.2	7.6	0.33499
17	5.3105	1.0769	12.8	7.6	2.9139
18	3.55	1	13.2	7.6	0.11221
19	3.35	0.85	13.2	7	0.33499
20	4.65	1	11	7.4	1.4126
21	2.5	0.6	16.2	7.8	0.631
22	3.85	0.88	13.2	7.6	0.7763
23	4	1	13.2	7	0.31625
24	3.55	0.85	13.2	7.6	0.53092
25	4	1	13.2	7.6	0.31625
26	3.25	0.8	13.2	7.2	0.44672
27	4.35	1	5	7.6	0.708
28	3.35	0.9	5	7.6	0.19954
29	3.35	0.9	5	7.6	0.19954
30	3.5	0.95	5	7.6	0.16789
31	3.5	0.9	5	7.6	0.28186
32[a]	4.8	1.07	55	7.6	0.96612

[a] Common between area and line sources

Table S9 Line source parameters (Askari and Mahsuli 2020)

Source number *i* per Fig. 5	Fault Name	a_i	b_i'	$d_{lower,i}$ (km)	$d_{upper,i}$ (km)	M_i^{max} (M_w)	$\lambda_{o,i}$
1	Doruneh	3.2574	0.90935	20	0	7.8	0.018028
2	South Parandak	3.2619	0.90935	20	1	7.3	0.018217
3	Astaneh-1	3.1591	0.90935	20	0	7.5	0.014379
4	Zefreh	3.4527	0.90935	20	1	7.6	0.028269
5	Firuzkuh	3.2211	0.90935	20	1	7.3	0.016585
6	Taleghan	3.4451	0.90935	20	1	7.2	0.027778
7	Kahrizak	3.2571	0.90935	20	1	6.8	0.018017
8	Mosha	3.3528	0.90935	20	1	7.6	0.02246
9	Alamutrud	3.5914	0.90935	20	1	7.7	0.038906
10	Khazar-1	3.3101	0.90935	20	1	7.7	0.020357
11	Lahijan	3.4544	0.90935	20	1	7.2	0.028381
12	HZF	4.9522	1.0801	20	5	7.7	0.10267
13	North Alborz-1	3.4101	0.90935	20	1	7.6	0.025625
14	Indes	3.7056	0.90935	20	1	7.6	0.050604
15	Rudbar	3.203	0.90935	20	1	7.3	0.015907
16	Kandovan	3.1466	0.90935	20	1	7.3	0.01397
17	North Qazvin	3.3436	0.90935	20	1	7.3	0.021986
18	North Tehran-1	3.4528	0.90935	20	1	7.2	0.028275
19	Eshtehard	3.2932	0.90935	20	1	7.2	0.01958
20	Siah Kuh-1	3.1983	0.90935	20	0	7.3	0.015736
21	Parandak	3.1402	0.90935	20	0	7.3	0.013765
22	Garmsar	3.3367	0.90935	20	0	7.5	0.021642
23	Pishva	3.0596	0.90935	20	1	6.8	0.011434
24	Kushk-e-Nosrat-1	3.4552	0.90935	20	1	7.5	0.028433
25	Eyvanekey	3.0583	0.90935	20	1	6.9	0.011398
26	Banan	3.1767	0.90935	20	1	7.4	0.014972
27	Torud	3.2853	0.90935	20	0	7.3	0.019225
28	Zanjan	3.424	0.90935	20	1	7.3	0.026461
29	Soltaniyeh	3.6042	0.90935	20	1	7.3	0.040072
30	North Alborz-2	3.5392	0.90935	20	1	7.6	0.034496
31	Khazar-2	3.3554	0.90935	20	1	7.7	0.022592
32	Siah Kuh-2	3.1702	0.90935	20	0	7.3	0.01475
33	Abdarreh	3.3854	0.90935	20	1	7.1	0.02421
34	Astaneh-2	3.5685	0.90935	20	0	7.1	0.036904
35	Atari-1	3.2766	0.90935	20	1	7.2	0.018847
36	Damghan	3.2222	0.90935	20	0	7.3	0.016625
37	Kuh-e-Gachab	3.2053	0.90935	20	1	7.4	0.015991
38	Kuh-e-Gugerd	3.1695	0.90935	20	1	7.3	0.014725
39	Kushk-e-Nosrat-2	3.2491	0.90935	20	1	7	0.017689
40	North Tehran-2	3.252	0.90935	20	1	7	0.017807
41	Arad	3.26	0.90935	20	0	6.9	0.018137
42	North Alborz-3	3.3021	0.90935	20	0	7.7	0.019986
43	Khazar-3	3.1989	0.90935	20	0	7.3	0.015758
44	Atari-2	3.2883	0.90935	20	0	7.4	0.019358
45	Astaneh-3	3.264	0.90935	20	1	7.1	0.018306

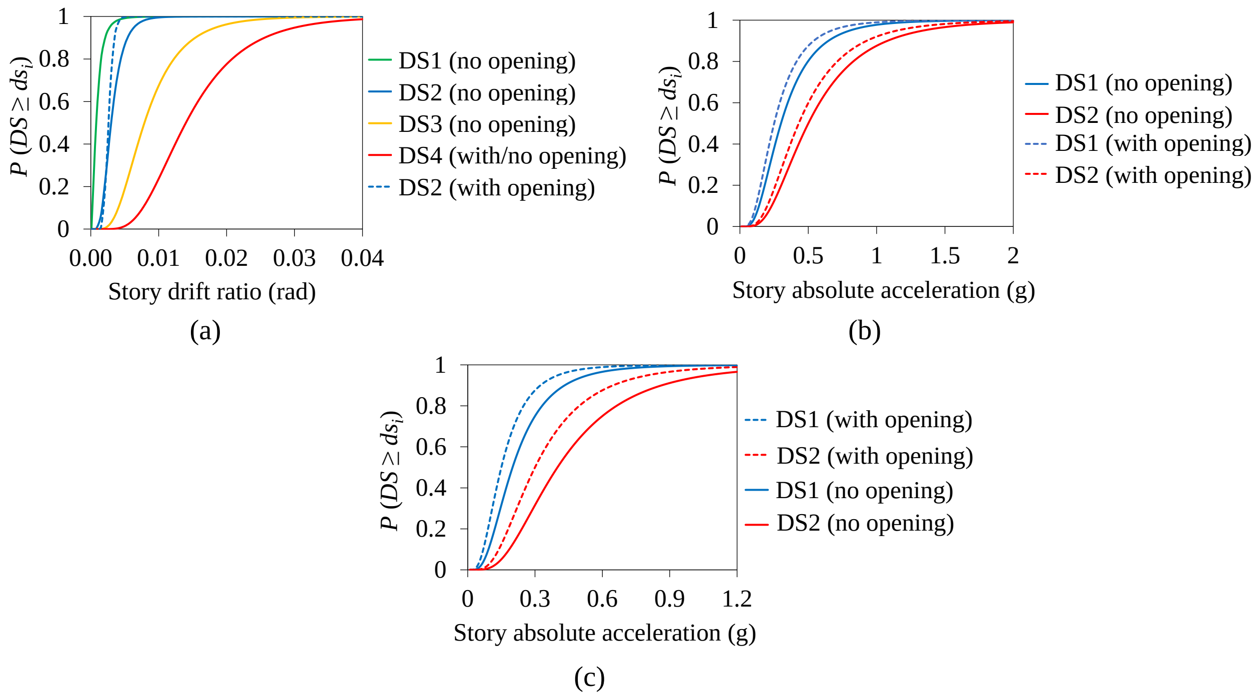

Fig. S8 Fragility curves for the (a) in-plane and (b) out-of-plane behavior of masonry infill walls (Cardone and Perrone 2015; De Risi et al. 2018), and (c) fragility curves for masonry façades (Khalili 2019); *DS* represents the damage state variable

References

AISC (2010) Specification for Structural Steel Buildings. ANSI/AISC 360-10, Chicago, Illinois

Askari M, Mahsuli M (2020) Modeling of Epistemic Uncertainties in Seismic Hazard Analysis Based on Reliability Methods. Technical Report, Center for Infrastructure Sustainability and Resilience Research, Sharif University of Technology, Tehran, Iran

Cardone D, Perrone G (2015) Developing Fragility Curves and Loss Functions for Masonry Infill Walls. Earthq Struct 9:257–279. https://doi.org/10.12989/eas.2015.9.1.000

De Risi MT, Del Gaudio C, Ricci P, Verderame GM (2018) In-Plane Behaviour and Damage Assessment of Masonry Infills with Hollow Clay Bricks in RC Frames. Eng Struct 168:257–275. https://doi.org/10.1016/j.engstruct.2018.04.065

Filippou FC, Popov EP, Bertero VV (1983) Effects of Bond Deterioration on Hysteretic Behavior of Reinforced Concrete Joint. Report No. UCB/EERC-83/19, Earthquake Engineering Research Center, University of California at Berkeley, Berkeley, CA

Gutenberg B, Richter CF (1944) Frequency of Earthquakes in California. Bull Seismol Soc Am 34:185–188

Hsiao PC, Lehman DE, Roeder CW (2012) Improved Analytical Model for Special Concentrically Braced Frames. J Constr Steel Res 73:80–94. https://doi.org/10.1016/j.jcsr.2012.01.010

Ibarra LF, Krawinkler H (2005) Global Collapse of Frame Structures Under Seismic Excitations. Report No. TB 152, The John A. Blume Earthquake Engineering Center, Stanford University, Stanford, CA

Ibarra LF, Medina RA, Krawinkler H (2005) Hysteretic Models That Incorporate Strength and Stiffness Deterioration. Earthq Eng Struct Dyn 34:1489–1511. https://doi.org/10.1002/eqe.495

Karamanci E (2013) Collapse Assessment and Performance-Based Evaluation Techniques for Concentrically Braced Frames Designed in Seismic Regions. Master of Engineering Thesis, Dept of Civil Eng and Appl Mech, McGill University, Montreal, Canada

Karamanci E, Lignos DG (2014) Computational Approach for Collapse Assessment of Concentrically Braced Frames in Seismic Regions. J Struct Eng 140:A4014019. https://doi.org/10.1061/(ASCE)ST.1943-541X.0001011

Khalili M (2019) Value-Based Seismic Performance Assessment of Common Masonry Façades in Iran. M.Sc. Thesis, Dept of Civil and Environ Eng, Sharif University of Technology, Tehran, Iran

Kim DW, Blaney C, Uang CM (2015) Panel Zone Deformation Capacity as Affected by Weld Fracture at Column Kinking Location. Eng J 52:27–46

Lignos DG, Hartloper AR, Elkady A, et al (2019) Proposed Updates to the ASCE 41 Nonlinear Modeling Parameters for Wide-Flange Steel Columns in Support of Performance-Based Seismic Engineering. J Struct Eng 145:04019083. https://doi.org/10.1061/(ASCE)ST.1943-541X.0002353

Lignos DG, Hikino T, Matsuoka Y, Nakashima M (2013) Collapse Assessment of Steel Moment Frames Based on E-Defense Full-Scale Shake Table Collapse Tests. J Struct Eng 139:120–132. https://doi.org/10.1061/(ASCE)ST.1943-541X.0000608

Lignos DG, Krawinkler H (2013) Development and Utilization of Structural Component Databases for Performance-Based Earthquake Engineering. J Struct Eng 139:1382–1394. https://doi.org/10.1061/(ASCE)ST.1943-541X.0000646

Lignos DG, Krawinkler H (2011) Deterioration Modeling of Steel Components in Support of Collapse Prediction of Steel Moment Frames Under Earthquake Loading. J Struct Eng 137:1291–1302. https://doi.org/10.1061/(ASCE)ST.1943-541X.0000376

Lignos DG, Krawinkler H (2010) A Steel Database for Component Deterioration of Tubular Hollow Square Steel Columns Under Varying Axial Load for Collapse Assessment of Steel Structures Under Earthquakes. In: 7th Int. Conf. on Urban Earthquake Engineering. Center for Urban Earthquake Engineering, Tokyo Institute of Technology, Tokyo, Japan

Mahsuli M, Rahimi H, Bakhshi A (2019) Probabilistic Seismic Hazard Analysis of Iran Using Reliability Methods. Bull Earthq Eng 17:1117–1143. https://doi.org/10.1007/s10518-018-0498-2

Manson SS (1965) Fatigue: A Complex Subject—Some Simple Approximations. Exp Mech 5:193–226

NIST (2017) Guidelines for Nonlinear Structural Analysis for Design of Buildings. Part IIa – Steel Moment Frames. NIST GCR 17-917-46v2, Prepared by Applied Technology Council, Prepared for National Institute of Standards and Technology, Gaithersburg, MD

Rahimi H, Mahsuli M (2019) Structural Reliability Approach to Analysis of Probabilistic Seismic Hazard and Its Sensitivities. Bull Earthq Eng 17:1331–1359. https://doi.org/10.1007/s10518-018-0497-3

Stoakes CD, Fahnestock LA (2011) Cyclic Flexural Testing of Concentrically Braced Frame Beam-Column Connections. J Struct Eng 137:739–747. https://doi.org/10.1061/(ASCE)ST.1943-541X.0000326

Uriz P, Mahin SA (2008) Towards Earthquake-Resistant Design of Concentrically Braced Steel-Frame Structures. PEER Report 2008/08, PEER Center, University of California at Berkeley, Berkeley, CA

Zareian F, Krawinkler H (2009) Simplified Performance-Based Earthquake Engineering. Report No. 169, The John A. Blume Earthquake Engineering Center, Dept of Civil and Environ Eng, Stanford University, Stanford, CA